Discrete unified gas kinetic scheme for all Knudsen number flows. IV. Strongly inhomogeneous fluids

Baochao Shan,[1] Peng Wang,[1] Yonghao Zhang,[2] and Zhaoli Guo[1,*]

[1]*State Key Laboratory of Coal Combustion, Huazhong University of Science and Technology, Wuhan, Hubei 430000, China*

[2]*James Weir Fluids Laboratory, Department of Mechanical and Aerospace Engineering, University of Strathclyde, Glasgow G1 1XJ, United Kingdom*

(Received 3 December 2019; accepted 2 March 2020; published 8 April 2020)

This work is an extension of the discrete unified gas kinetic scheme (DUGKS) from rarefied gas dynamics to strongly inhomogeneous dense fluid systems. The fluid molecular size can be ignored for dilute gases, while the nonlocal intermolecular collisions and the competition of solid-fluid and fluid-fluid interactions play an important role for surface-confined fluid flows at the nanometer scale. The nonequilibrium state induces strong fluid structural-confined inhomogeneity and anomalous fluid flow dynamics. According to the previous kinetic model [Guo *et al.*, Phys. Rev. E **71**, 035301(R) (2005)], the long-range intermolecular attraction is modeled by the mean-field approximation, and the volume exclusion effect is considered by the hard-sphere potential in the collision operator. The kinetic model is solved by the DUGKS, which has the characteristics of asymptotic preserving, low dissipation, second-order accuracy, and multidimensional nature. Both static fluid structure and dynamic flow behaviors are calculated and validated with Monte Carlo or molecular dynamics results. It is shown that the flow of dense fluid systems tends to that of rarefied gases as the dense degree decreases or the mean flow path increases. The DUGKS is proved to be applicable to simulate such nonequilibrium dense fluid systems.

DOI: 10.1103/PhysRevE.101.043303

I. INTRODUCTION

The hydrodynamics of nanoscale fluid systems exhibits many peculiar behaviors compared to that at the macroscopic level [1], which has drawn growing interest in the research of lab-on-a-chip [2], storage, conversion and exploitation of energy [3–6], water purification [7,8], nanomanufacturing [9,10], carbon sequestration in metal organic frameworks [11], gas separation [12,13], and so on. Although the particle-based molecular dynamics (MD) and direct simulation of Monte Carlo (DSMC) have been commonly used to study such systems, these techniques are usually computationally intensive [1], and suffer huge statistical noise, especially for flows near the equilibrium state [14] or in the high-density regime [15]. Therefore, a numerical scheme with high accuracy and applicability to a wide range of flow regimes is desirable for the study of nanometer scale fluid flows.

The Knudsen number (Kn), which is defined as the ratio of fluid molecular mean free path (MFP) to the characteristic length of flow field [14], is normally taken as the criterion number to characterize flow regimes from the continuum flow ($\mathrm{Kn} < 0.001$) to the free molecular flow ($\mathrm{Kn} > 10$) in rarefied gas dynamics. The Navier-Stokes (NS) equation can be adopted to simulate fluid flow in the continuum flow regime, while the NS equation with slip boundary condition is usually employed in the slip flow regime ($0.001 < \mathrm{Kn} < 0.1$), where the rarefaction effects can no longer be neglected [5,16–18]. However, the NS equation (with slip boundary condition) fails to capture the nonequilibrium effects in more rarefied flow regimes, e.g., the transition and free molecular flow regimes, where the continuum assumption becomes totally invalid [15]. Besides, it also fails when fluid properties or transport coefficients vary significantly over a molecular size [19]. Consequently, the NS equation cannot be employed to capture nanoscale fluid behavior, since both cases may happen in a dense fluid system at the nanometer scale.

The Boltzmann equation is well recognized to work in all the flow regimes ranging from continuum flow to free molecular flow [20,21]. However, it is only valid for dilute gases with homogeneous properties, i.e., satisfying the following conditions: (1) ignorable molecular size; (2) localized binary collision between molecules; (3) molecular chaos hypothesis [1,15,22]. For a dense fluid system at the nanometer scale, molecular size cannot be ignored since it is comparable to the characteristic length or the MFP. Thus, the Boltzmann equation breaks down for such systems.

The Boltzmann equation was extended into dense gas system by Enskog [23] and later modified by Van Beijeren and Ernst [24], known as the Enskog theory and the revised Enskog theory, respectively. Although molecular size and the collisional transfer of momentum and energy (nonlocal collisions) are considered in such theory, it still assumes molecular chaos and uses the rigid spherical model [23]. In addition, molecular interactions (fluid-fluid and fluid-solid) become predominant on dynamical and structural properties of dense fluids in the nanoscale fluid flows. Therefore, the Enskog theory is also not sufficient to describe the state of a dense fluid system at the nanometer scale. To overcome this limitation, the effects of a long-range smooth attractive tail is added to the hard-core repulsion of the Enskog equation, known as the Enskog-Vlasov equation [25–27], to model the intermolecular potential effects in dense fluids, where the long-range interactions are dealt with by a collective mean field.

*zlguo@hust.edu.cn

Based on the Enskog-Vlasov equation, the nanoscale fluid flow is studied by Davis [28] and Vanderlick and co-workers [29,30], where the kinetic equation yields the exact Yvon-Born-Green equations for the density distributions at equilibrium. The molecular size, nonlocal collisions, and molecular interactions (fluid-solid and fluid-fluid) were simultaneously considered. However, the collision operator in their theory is quite difficult in practical applications. Later, a tractable kinetic model was proposed by Guo *et al.* [22] to account for the strong inhomogeneity in dense fluid systems. Following the Chapman-Enskog analysis, the original kinetic equation was employed to study the equilibrium and dynamic behaviors of confined fluids on the macroscale level. However, only the no-slip cases were studied in their paper. Besides, the hydrodynamic equation [22] is only applicable to continuum flows, since it retains up to the first-order terms in the Chapman-Enskog series. Thus, the nonequilibrium effects are not properly captured. In this study, the discrete unified gas-kinetic scheme (DUGKS) [31] is extended to solve the kinetic model [22] for strongly inhomogeneous confined fluid systems, which can capture the rarefaction effects as well.

Combining the advantages of the lattice Boltzmann method (LBM) [32] and the unified gas kinetic scheme (UGKS) [15], the DUGKS [31] was proposed recently for rarefied gas flows, which is applicable to the entire flow regimes. It has been successfully applied to low-speed isothermal flows ranging from the continuum to free molecular flow regimes [31], compressible flows considering heat transfer and shock discontinuity [33], flows of binary gas mixtures [14], Boussinesq flows [34], multiscale heat transfer [35–37], thermally induced nonequilibrium flows [38], rarefied gas flow in microchannels [39], solid-liquid phase change problems [40], immiscible two phase flows [41] etc. The capability of the DUGKS to tackle multiscale problems has been thoroughly discussed in these studies, and a rigorous theoretical analysis of its unified preserving properties was also made recently [42]. However, the DUGKS is based on the Boltzmann equation, which is not sufficient for dense fluid systems with strong inhomogeneity at the nanometer scale [1,4,9,22].

The purpose of this paper is to extend the DUGKS to nonequilibrium dense fluid systems with strong inhomogeneity at the nanometer scale based on the kinetic model [22], where the effects of volume exclusion and long-range fluid-fluid and fluid-wall interactions are simultaneously taken into account.

II. KINETIC MODEL FOR NANOSCALE DENSE FLUID SYSTEM

The Enskog theory considers the effects of finite size of molecules and nonlocal collisions of hard-sphere fluids [4,23], which are ignored in the Boltzmann equation. Combining the Enskog equation and the mean-field theory to account for the volume exclusion effects and the long-range intermolecular attractions, respectively, the evolution of velocity distribution function for a dense fluid can be described by the following kinetic equation [22]

$$\partial_t f + \boldsymbol{\xi}\cdot\nabla_{\boldsymbol{r}} f - m^{-1}\nabla_{\boldsymbol{r}}(\phi_{\rm ext}+\phi_m)\cdot\nabla_{\boldsymbol{\xi}} f = \Omega(f), \tag{1}$$

where $f(\boldsymbol{r},\boldsymbol{\xi},t)$ is the velocity distribution function of molecular velocity $\boldsymbol{\xi}$ at spatial position $\boldsymbol{r}$ and time t; ∂_t represents the partial derivative in terms of time t; m is the molecular mass; $\nabla_{\boldsymbol{r}}$ and ∇_{ε} represent gradient operators in terms of space $\boldsymbol{r}$ and velocity $\boldsymbol{\xi}$, respectively; $\phi_{\rm ext}$ is the external potential term; ϕ_m relates to the attractive part of the fluid-fluid potential; and $\Omega(f)$ is the extended Enskog collision operator. Following the projection method for hard-sphere fluids [9,43], $\Omega(f)$ can be further divided as the superposition of a Boltzmann collision term Ω_B and an excess collision term Ω_E. The Boltzmann part Ω_B is modeled by the Bhatnagar-Gross-Krook (BGK) relaxation process [22],

$$\Omega_B = -\frac{f-f^{eq}}{\tau}, \tag{2}$$

where τ is the relaxation time, and f^{eq} is the Maxwellian local equilibrium distribution function,

$$f^{eq} = n\left(\frac{1}{2\pi RT}\right)^{3/2}\exp\left[-\frac{(\boldsymbol{\xi}-\boldsymbol{u})^2}{2RT}\right], \tag{3}$$

where n is the number density, R is the gas constant, T is the constant temperature of the isothermal system, and $\boldsymbol{u}$ is the flow velocity. The macroflow variables can be calculated from the moments of the distribution function,

$$n = \int f d\boldsymbol{\xi}, \quad \boldsymbol{u} = n^{-1}\int \boldsymbol{\xi} f d\boldsymbol{\xi}. \tag{4}$$

Note that only the isothermal case is considered in this paper, and the temperature is given as a constant. The excess collision term Ω_E accounting for volume exclusion effects of intermolecular repulsion is expressed as [22]

$$\Omega_E = -V_0 f^{eq}(\boldsymbol{\xi}-\boldsymbol{u})\cdot[2\mathbf{A}\chi(\bar{n})+\mathbf{B}\bar{n}], \tag{5}$$

where V_0 is related to molecular diameter σ, i.e., $V_0 = 2\pi\sigma^3/3$ [23,44]; $\bar{n} = \int w(\boldsymbol{r}')n(\boldsymbol{r}+\boldsymbol{r}')d\boldsymbol{r}'$ is the local average density (LAD) with $w(\boldsymbol{r})$ being a weight function [45], which was commonly used in the free energy density functional theory (DFT) to study inhomogeneous fluid systems [29,45]; χ is the radial distribution function (RDF) for homogeneous hard-sphere fluids [46]. To account for the inhomogeneity of a dense fluid system, the RDF χ in Eq. (5) is evaluated with the LAD, rather than the local density n. Meanwhile, the parameters $\boldsymbol{A}$ and $\boldsymbol{B}$ are two gradient operators defined by [22]

$$\mathbf{A} = \frac{1}{D}\int_{|\boldsymbol{r}'|<\sigma/2}\boldsymbol{r}'\bar{n}(\boldsymbol{r}+\boldsymbol{r}')d\boldsymbol{r}', \tag{6}$$

and

$$\mathbf{B} = \frac{1}{D}\int_{|\boldsymbol{r}'|<\sigma/2}\boldsymbol{r}'\chi[\bar{n}(\boldsymbol{r}+\boldsymbol{r}')]d\boldsymbol{r}', \tag{7}$$

where σ is the effective molecular diameter, and D is equal to $\pi\sigma^5/120$.

The external potential $\phi_{\rm ext}$ includes all external potentials, such as the wall potential ϕ_w and that driving the fluid to flow. The wall potential can be represented by the 10-4-3 potential for a planar wall [29],

$$\phi_w(z) = 2\pi\varepsilon_{wf}\left[\frac{2}{5}\left(\frac{\sigma_{wf}}{z}\right)^{10} - \left(\frac{\sigma_{wf}}{z}\right)^4 - \frac{\sigma_{wf}^4}{3\Delta(z+0.61\Delta)^3}\right],$$
$$\Delta = \sigma_{wf}/\sqrt{2}, \tag{8}$$

or the 10-4 potential [47],

$$\phi_w(z) = 2\pi\varepsilon_{wf}\left[\frac{2}{5}\left(\frac{\sigma_{wf}}{z}\right)^{10} - \left(\frac{\sigma_{wf}}{z}\right)^{4}\right], \tag{9}$$

where ε_{wf} and σ_{wf} are the energy and range parameters of wall-fluid interactions, respectively, and z is the perpendicular distance from the wall. Note that the 10-4-3 wall potential is a result of the integration of a continuous distribution of all the solid molecules interacting with gas molecules through the 12-6 Lennard-Jones (LJ) potential. Consequently, the 10-4-3 wall potential is approximately equivalent to the 12-6 potential of fluid-solid molecules in the MD simulations. For more general geometrics, the potential at a position can be measured from those of all solid molecules. The empirical parameters between the interactive molecules are chosen exactly the same as those in the MD simulations.

The mean-field theory is adopted to account for the long-range intermolecular attraction, where a gas molecule is considered to move under the average attraction of molecules in the system [48]. According to the decomposition principle of the pairwise intermolecular potential [49], the molecular interaction part acts when the distance between molecules is larger than the effective diameter σ, and thus ϕ_m in Eq. (1) can be expressed as

$$\phi_m(\boldsymbol{r}) = \int_{|\boldsymbol{r}'|>\sigma} n(\boldsymbol{r}+\boldsymbol{r}')\phi_{\rm att}(|\boldsymbol{r}'|)d\boldsymbol{r}', \tag{10}$$

where $\phi_{\rm att}$ is the attractive part of the Lennard-Jones (LJ) fluids, which can be represented as

$$\phi_{\rm att}(r) = \begin{cases} 0, & r < \sigma \\ 4\varepsilon_{ff}\left[\left(\frac{\sigma_{ff}}{r}\right)^{12} - \left(\frac{\sigma_{ff}}{r}\right)^{6}\right], & r > \sigma \end{cases}, \tag{11}$$

where ε_{ff} and σ_{ff} are the energy and range parameters of fluid-fluid interactions, respectively, and r is the distance between two fluid molecules. Meanwhile, the interaction range of wall atoms and fluid atoms can be represented by the effective diameter σ as [9,50]

$$\sigma \approx \frac{1 + a_1 T_r}{1 + a_2 T_r + a_3 T_r^2}, \tag{12}$$

where $T_r = k_B T/\varepsilon$ is the reduced temperature, with $a_1 = 0.2977$, $a_2 = 0.331\,63$, and $a_3 = 0.001\,047\,71$.

III. DUGKS FOR THE KINETIC MODEL

In this section, the DUGKS will be employed to solve the kinetic equation (1). Before implementation, a transformation is conducted on Eq. (1) for convenience,

$$\partial_t f + \boldsymbol{\xi}\cdot\nabla_{\boldsymbol{r}} f = \Omega_B + \boldsymbol{G}, \tag{13}$$

where $\boldsymbol{G}$ is a total force term as a combination of volume exclusion effects, long-range intermolecular attraction, surrounding wall potentials, and other outside forces, which in the current work can be expressed as

$$\boldsymbol{G} = -\{\nabla\phi_{\rm ext} + \nabla\phi_m + V_0 RT[2\mathbf{A}\chi(\bar{n}) + \mathbf{B}\bar{n}]\}\frac{\boldsymbol{\xi}-\boldsymbol{u}}{RT} f^{eq}, \tag{14}$$

where the derivative of distribution function f in terms of particle velocity $\nabla_{\boldsymbol{\xi}} f$ was approximated by its equilibrium state $\nabla_{\boldsymbol{\xi}} f^{eq}$, due to the fact that f^{eq} is the leading part of the distribution f and the gradient of f^{eq} has the most important contribution to the gradient of f [48], especially for high fluid density cases as in the current work

$$\nabla_{\boldsymbol{\xi}} f \approx \nabla_{\boldsymbol{\xi}} f^{eq} = -\frac{\boldsymbol{\xi}-\boldsymbol{u}}{RT} f^{eq}. \tag{15}$$

Since the original DUGKS does not include the external force term $\boldsymbol{G}$, we will update Eq. (13) by two steps: (1) employ the standard updating rules as originally described in [14,31,33] [see Secs. III A and III B]; (2) treat the external force term $\boldsymbol{G}$ by the Strang splitting technique [51–53] [see Sec. III C].

A. Updating in the standard DUGKS

For the original DUGKS without considering the external force term $\boldsymbol{G}$, Eq. (13) can be written as

$$\partial_t f + \boldsymbol{\xi}\cdot\nabla_{\boldsymbol{r}} f = \Omega_B. \tag{16}$$

Adopting the midpoint rule for time integration of the convection term, and the trapezoidal rule for the collision term of the evolution equation (16), we can discretize it into the following form for the cell j ($\boldsymbol{r}_j$ is the cell center) from time t_n to t_{n+1} as

$$f_j^{n+1} - f_j^n + \frac{\Delta t}{|V_j|}F^{n+1/2} = \frac{\Delta t}{2}\left(\Omega_j^{n+1} - \Omega_j^n\right), \tag{17}$$

where the superscript $(n+1)$ and n represent time t_{n+1} and t_n, respectively; the subscript j represents space $\boldsymbol{r}_j$ at the cell center, $F^{n+1/2}$ is the microflux across the cell interface, i.e.,

$$F^{n+1/2} = \int_{\partial V_j} (\boldsymbol{\xi}\cdot\boldsymbol{n}) f(\boldsymbol{r}, t_{n+1/2}) d\boldsymbol{S}, \tag{18}$$

where ∂V_j and $|V_j|$ are the cell surface and cell volume of the cell V_j, respectively; $\boldsymbol{n}$ is the outward unit vector normal to the surface.

By introducing two auxiliary distribution functions $\tilde{f}$ and $\tilde{f}^+$ as

$$\tilde{f} = f - \frac{\Delta t}{2}\Omega_B = \frac{2\tau+\Delta t}{2\tau} f - \frac{\Delta t}{2\tau} f^{eq}, \tag{19}$$

$$\tilde{f}^+ = f + \frac{\Delta t}{2}\Omega_B = \frac{2\tau-\Delta t}{2\tau+\Delta t}\tilde{f} + \frac{2\Delta t}{2\tau+\Delta t} f^{eq}, \tag{20}$$

Eq. (16) can be rewritten as

$$\tilde{f}_j^{n+1} = \tilde{f}_j^{+,n} - \frac{\Delta t}{|V_j|}F^{n+1/2}. \tag{21}$$

Since the BGK collision operator Ω_B satisfies the following conservative laws,

$$\int \Omega_B d\boldsymbol{\xi} = 0, \quad \int \boldsymbol{\xi}\Omega_B d\boldsymbol{\xi} = 0, \tag{22}$$

the evolution can be done explicitly according to Eq. (21) by tracking auxiliary distribution function $\tilde{f}$, instead of the original distribution function f. The density and velocity can be calculated as

$$n = \int \tilde{f} d\boldsymbol{\xi}, \quad n\boldsymbol{u} = \int \boldsymbol{\xi}\tilde{f} d\boldsymbol{\xi}. \tag{23}$$

B. Flux evaluation

In order to update $\tilde{f}$ from t_n to t_{n+1} according to Eq. (21), the microflux across the cell interface ∂V_j needs to be evaluated first, the key point of which is to reconstruct the original distribution function $f^{n+1/2}$ at time $t_{n+1/2}$ on the cell interface. Similar to the treatment in the above updating rule, we integrate Eq. (16) along the characteristic line within a half time step, i.e., $h = \Delta t/2$ with the trapezoidal rule for the collision term,

$$f(\boldsymbol{r}_{ij}, \boldsymbol{\xi}, t_n + h) - f(\boldsymbol{r}_{ij} - \boldsymbol{\xi}h, \boldsymbol{\xi}, t_n) = \frac{h}{2}[\Omega(\boldsymbol{r}_{ij}, \boldsymbol{\xi}, t_n + h) + \Omega(\boldsymbol{r}_{ij} - \boldsymbol{\xi}h, \boldsymbol{\xi}, t_n)], \quad (24)$$

where $\boldsymbol{r}_{ij}$ is the center of the cell interface between cell i and cell j.

By introducing two auxiliary distribution functions $\bar{f}$ and $\bar{f}^+$ expressed as

$$\bar{f} = f - \frac{h}{2}\Omega_B = \frac{2\tau + h}{2\tau} f - \frac{h}{2\tau} f^{eq}, \quad (25)$$

$$\bar{f}^+ = f + \frac{h}{2}\Omega_B = \frac{2\tau - h}{2\tau + h}\bar{f} + \frac{2h}{2\tau + h} f^{eq} = \frac{2\tau - h}{2\tau + \Delta t}\tilde{f} + \frac{3h}{2\tau + \Delta t} f^{eq}, \quad (26)$$

Equation (16) can be transformed into the following form:

$$\bar{f}(\boldsymbol{r}_{ij}, \boldsymbol{\xi}, t_{n+1/2}) = \bar{f}^+(\boldsymbol{r}_{ij} - \boldsymbol{\xi}h, \boldsymbol{\xi}, t_n). \quad (27)$$

According to Eqs. (22) and (25), the density and velocity can also be obtained from $\bar{f}$; i.e.,

$$n = \int \bar{f} d\boldsymbol{\xi}, \quad n\boldsymbol{u} = \int \boldsymbol{\xi} \bar{f} d\boldsymbol{\xi}. \quad (28)$$

Meanwhile, $\bar{f}^+$ and $\tilde{f}^+$ satisfy the following relationship, which will be used to evaluate the $\tilde{f}^+$ in Eq. (21):

$$\tilde{f}^+ = \tfrac{4}{3}\bar{f}^+ - \tfrac{1}{3}\tilde{f}. \quad (29)$$

Once $\bar{f}(\boldsymbol{r}_{ij}, \boldsymbol{\xi}, t_{n+1/2})$ is evaluated from Eq. (27), the original distribution function $f(\boldsymbol{r}_{ij}, \boldsymbol{\xi}, t_{n+1/2})$ at interface center $\boldsymbol{r}_{ij}$ can be calculated according to the relationship between $\bar{f}$ and f in Eq. (25), after which the microflux is obtained according to Eq. (18). Thus, the main task is to construct the $\bar{f}^+(\boldsymbol{r}_{ij} - \boldsymbol{\xi}h, \boldsymbol{\xi}, t_n)$ in Eq. (27), and to obtain $\bar{f}(\boldsymbol{r}_{ij}, \boldsymbol{\xi}, t_{n+1/2})$ consequently.

Generally, $\bar{f}^+(\boldsymbol{r}_{ij} - \boldsymbol{\xi}h, \boldsymbol{\xi}, t_n)$ can be expanded around $\bar{f}^+(\boldsymbol{r}_{ij}, \boldsymbol{\xi}, t_n)$ [31] or $\bar{f}^+(\boldsymbol{r}_i, \boldsymbol{\xi}, t_n)$ [33] by assuming a linear relationship. Considering a significant density oscillation may occur in a nanoscale dense fluid system, we will expand it around the cell center value and employ the Van Leer limiter [54]. The linear relationship and limiter can be expressed as

$$\bar{f}^+(\boldsymbol{r}_{ij} - \boldsymbol{\xi}h, \boldsymbol{\xi}, t_n) = \bar{f}^+(\boldsymbol{r}_j, \boldsymbol{\xi}, t_n) + [(\boldsymbol{r}_{ij} - \boldsymbol{\xi}h) - \boldsymbol{r}_j] \cdot \boldsymbol{\gamma}_j, \quad (\boldsymbol{r}_{ij} - \boldsymbol{\xi}h) \in V_j, \quad (30)$$

where $\boldsymbol{\gamma}_j$ is the corresponding slope at the cell V_j. Taking the component in the x direction, for example, the slope can be written as

$$\gamma_{j,x} = [\mathrm{sign}(s_1) + \mathrm{sign}(s_2)]\frac{|s_1||s_2|}{|s_1| + |s_2|}, \quad (31)$$

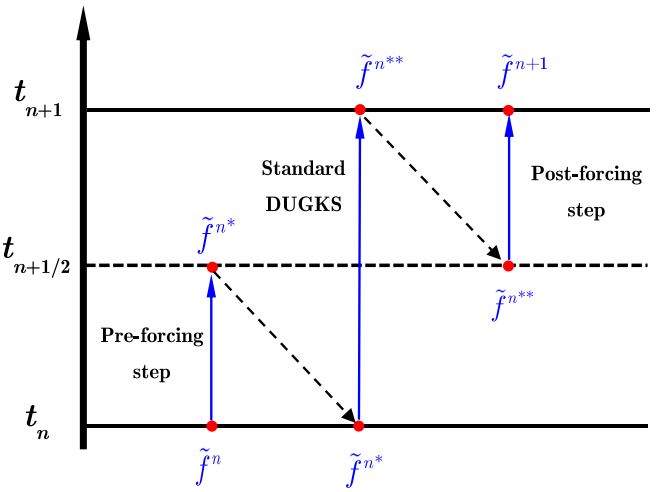

FIG. 1. The evolution procedure from time t_n to t_{n+1} in the Strang splitting method. f^{n*} and f^{n**} represent the solutions from the preforcing step and the standard DUGKS, respectively.

where

$$s_1 = \frac{\bar{f}^+(x_j) - \bar{f}^+(x_{j-1})}{x_j - x_{j-1}}, \quad s_2 = \frac{\bar{f}^+(x_{j+1}) - \bar{f}^+(x_j)}{x_{j+1} - x_j}. \quad (32)$$

Up to now, all the variables needed for the evolution equation, i.e., Eq. (21), are solved, where the external force term $\boldsymbol{G}$ is not included. The Strang splitting algorithm [51] will be introduced below regarding how to couple the external force term $\boldsymbol{G}$ into the standard DUGKS evolution [52,53] as described above.

C. Strang splitting method for external force

In the Strang splitting method, a half time step integration is implemented on distribution functions before and after the standard DUGKS procedure, which is called the preforcing and postforcing step, respectively. The preforcing step, the standard DUGKS and the postforcing step can be respectively written as

$$\partial_t f = 0.5\boldsymbol{G}, \quad (33)$$

$$\partial_t f + \boldsymbol{\xi} \cdot \nabla_{\boldsymbol{r}} f = \Omega_B, \quad (34)$$

$$\partial_t f = 0.5\boldsymbol{G}. \quad (35)$$

The evolution from time t_n to t_{n+1} in the Strang splitting algorithm can be seen in Fig. 1.

In the preforcing and/or postforcing step, integrating Eqs. (33) and/or (35) over a time step Δt, we have

$$f^* = f + \frac{\Delta t}{2}\boldsymbol{G}(n, \boldsymbol{u}), \quad (36)$$

where f^* is a solution from the preforcing or postforcing step.

According to Eq. (19), we have the following relations,

$$\tilde{f} = \frac{2\tau + \Delta t}{2\tau} f - \frac{\Delta t}{2\tau} f^{eq}(n, \boldsymbol{u}), \quad (37)$$

$$\tilde{f}^* = \frac{2\tau + \Delta t}{2\tau} f^* - \frac{\Delta t}{2\tau} f^{eq}(n^*, \boldsymbol{u}^*), \quad (38)$$

where the density and velocity can be calculated as

$$n^* = n, \quad \boldsymbol{u}^* = \boldsymbol{u} + 0.5\boldsymbol{G}\Delta t. \tag{39}$$

Coupling Eqs. (36)–(38), $\tilde{f}^*$ can be calculated from $\tilde{f}$ by the following equation:

$$\tilde{f}^* = \tilde{f} + \frac{\Delta t}{2\tau}[f^{eq}(n,\boldsymbol{u}) - f^{eq}(n^*,\boldsymbol{u}^*)] + \frac{(2\tau+\Delta t)\Delta t}{4\tau}\boldsymbol{G}(n,\boldsymbol{u}). \tag{40}$$

D. Relaxation time

Based on the LAD method [55], the relaxation time τ in the collision operator Ω_B of Eq. (2) is determined by

$$\tau = \frac{\mu(\bar{n})}{nk_BT}, \tag{41}$$

where k_B is the Boltzmann constant, and $\mu(\bar{n})$ is the viscosity of homogeneous dense fluid evaluated at the LAD $\bar{n}$ expressed as [23]

$$\mu(\bar{n}) = \frac{5.0}{16\sigma^2}\sqrt{\frac{k_BT}{\pi}}\bar{n}V_0(Y^{-1} + 0.8 + 0.7614Y), \tag{42}$$

where the parameter Y and the radial distribution function χ are calculated by [44–46]

$$Y = \bar{n}V_0\chi(\bar{n}), \quad \chi(\bar{n}) = \frac{1-0.5\eta}{(1-\eta)^3}, \quad \eta = \frac{\bar{n}V_0}{4}. \tag{43}$$

E. Boundary condition

In the kinetic models, appropriate boundary conditions should be given for the distribution functions at the solid walls [31]. The surface slip significantly depends on the relative strength between fluid-wall and fluid-fluid interactions, which can be characterized by the ratio of energy parameter ε_{wf} to ε_{ff} [56]. With the decrease of the ratio $\varepsilon_{wf}/\varepsilon_{ff}$, the boundary transforms from wetting to nonwetting, and the slip increases correspondingly. In this study, the bounce-back boundary condition is employed for a no-slip boundary condition to simulate the wetting cases, where gas molecules adsorb on the wall and form an adsorption layer when hitting the solid molecules, rather than the usual diffuse or specular reflection. The slip boundary condition for the nonwetting cases can also be achieved by the bounce-back boundary condition with a slip velocity, which is determined by the fluid-solid interactions. Note that, even in the nonwetting case, weak adsorption layers may form near the wall, as shown in Fig. 8(b). In this paper, we mainly focus on the wetting case with a no-slip boundary condition, and the detailed bounce-back scheme can be found in Guo *et al.* [31].

F. Algorithm

The standard procedure of the DUGKS from time t_n to t_{n+1} is the same as the previous study [33]. The difference lies in how to couple the external force $\boldsymbol{G}$ by the Strang splitting technique with the standard DUGKS [52,53], as shown in Fig. 1. Detailed computational procedures can be summarized in the following steps:

(1) Preforcing step calculation with a half time step $h = \Delta t/2$.

(a) Determine the local average density $\bar{n}$, which can be found in Bitsanis *et al.* [57], Tarazona [45], or Vanderlick *et al.* [29].

(b) Calculate the radial distribution function χ according to Eq. (43).

(c) Compute the gradients of the radial distribution function and local average density according to Eqs. (6) and (7), respectively.

(d) Coupling the force term $\boldsymbol{G}$ into the Strang splitting algorithm according to Eq. (40).

(2) The standard DUGKS evolution from time t_n to t_{n+1}.

(a) Calculate $\bar{f}^+$ from $\tilde{f}$ at the cell interface according to Eq. (26).

(b) Compute the gradient of $\bar{f}^+$ in each cell according to Eq. (31).

(c) Calculate the distribution function $\bar{f}^+$ at $(\boldsymbol{r}_{ij} - \boldsymbol{\xi}h)$ according to Eq. (30).

(d) Determine the distribution function $\bar{f}$ at the cell interface and time $t_{n+1/2}$ according to Eq. (27).

(e) Calculate the conserved flow variables from $\bar{f}$ according to Eq. (28).

(f) Determine the original distribution function f at cell interface and time $t_{n+1/2}$ from $\bar{f}(\boldsymbol{r}_{ij}, \boldsymbol{\xi}, t_{n+1/2})$ and $f^{eq}(\boldsymbol{r}_{ij}, \boldsymbol{\xi}, t_{n+1/2})$ according to Eq. (25).

(g) Calculate the flux $\boldsymbol{F}^{n+1/2}$ through each cell interface from $f^{n+1/2}$ according to Eq. (18).

(h) Determine $\tilde{f}^+$ at the cell center and time t_n according to Eq. (29).

(i) Update the cell-averaged $\tilde{f}$ in each cell from t_n to t_{n+1} according to Eq. (21).

(3) Postforcing step (the same as the preforcing step).

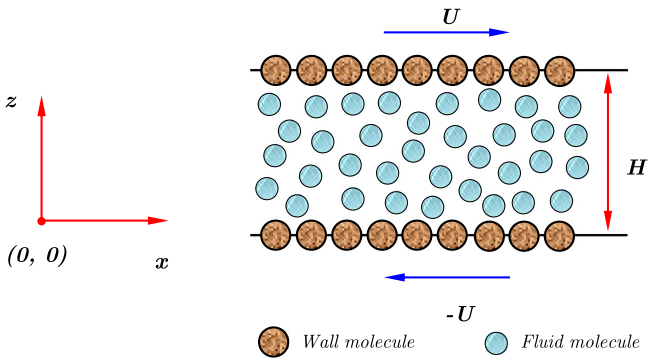

FIG. 2. Fluid molecules confined between two parallel plates at the nanometer scale.

IV. MODEL VALIDATION

In this part, the static fluid structure and flow behaviors of dense fluid systems confined between two plates with a separation of H at the nanometer scale, as sketched in Fig. 2, are studied. For such a system, the fluid molecular size can no longer be neglected comparing to the channel width H,

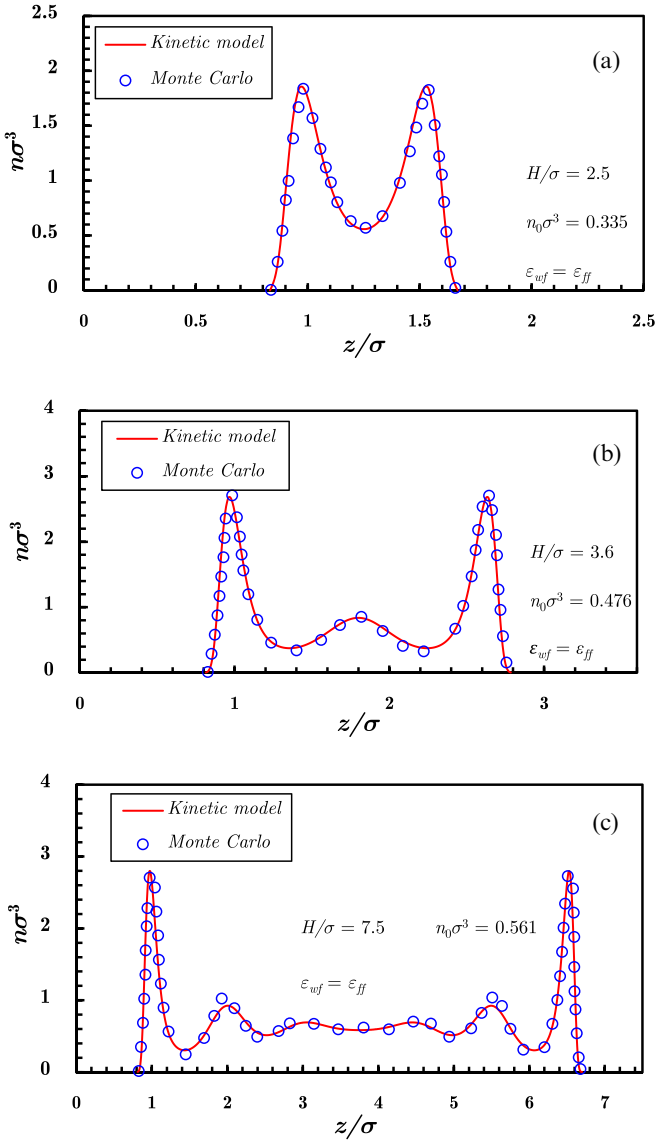

FIG. 3. Density distributions of LJ fluids confined between two parallel plates with 10-4-3 LJ potential at the temperature of $T = 1.2\ \varepsilon_{ff}/k_B$; Monte Carlo results can be found in Ref. [58].

which means that the Boltzmann equation fails under this circumstance.

A. Static fluid structure

The equilibrium structure of the LJ fluids with three different channel widths is first tested. In the simulation, the 10-4-3 LJ potential is exerted on the fluid molecules by the top and bottom plates, while the 12-6 LJ potential is employed for fluid molecular interactions. The channel widths and pore-averaged density, which is defined as $n_0 = \int_0^H n(y)dy/H$, are displayed in Fig. 3, while the fluid system temperature is taken as $T_r = 1.2$ for all three cases. Meanwhile, the solid-fluid energy parameter ε_{wf} equals fluid-fluid energy parameter ε_{ff}, meaning the strengths of solid-fluid interactions and fluid-fluid interactions are approximately the same.

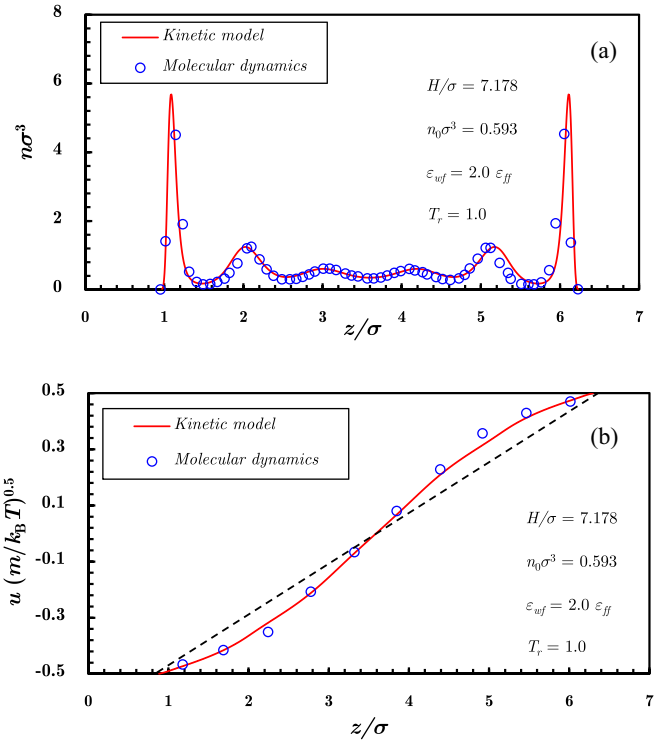

FIG. 4. Density (a) and velocity (b) profiles of Couette flow for LJ fluids in confined plates with 10-4 potential. MD results can be found in Ref. [55]. The dotted line in the bottom panel represents the linear distribution of the velocity profile predicted by the conventional hydrodynamic model, which ignores the competition between the fluid-fluid and fluid-solid interactions.

As shown in Fig. 3, the density profiles in all the cases oscillates significantly across the channel due to the combined effects of external wall potential, volume exclusion effects, and long-range intermolecular interactions. The unique density structures agree well with the Monte Carlo results [58] in all three cases, including the magnitudes and locations of peaks as well as their oscillation tendency. No bulk regions appear for these narrow channels, i.e., $H = 2.5\sigma$ [Fig. 3(a)] and $H = 3.6\sigma$ [Fig. 3(b)], while the fluid will become homogeneous near the center region with the increase of channel width [Fig. 3(c)]. Due to the strong repulsion from the solid molecules, it is hard for fluid molecules to approach the boundary and there will be a vacuum layer between the first fluid layer and the wall, with the thickness equaling δ. The capability of capturing the critical changes in fluid structure reveals the applicability of the present DUGKS in predicting the fluid structure induced by external wall potential and fluid molecular interactions.

B. Dynamic behaviors

1. Couette flow

The second test case is the Couette flow, with the top and bottom plates moving with a velocity of $U = 0.5\sqrt{k_BT/m}$ in the x and $-x$ directions, respectively, as shown in Fig. 2. In the computation, the grid size in the y direction is set to be $\Delta y = 0.01\sigma$, which is fine enough to produce grid independent solutions. Meanwhile, eight Gauss-Hermite discrete

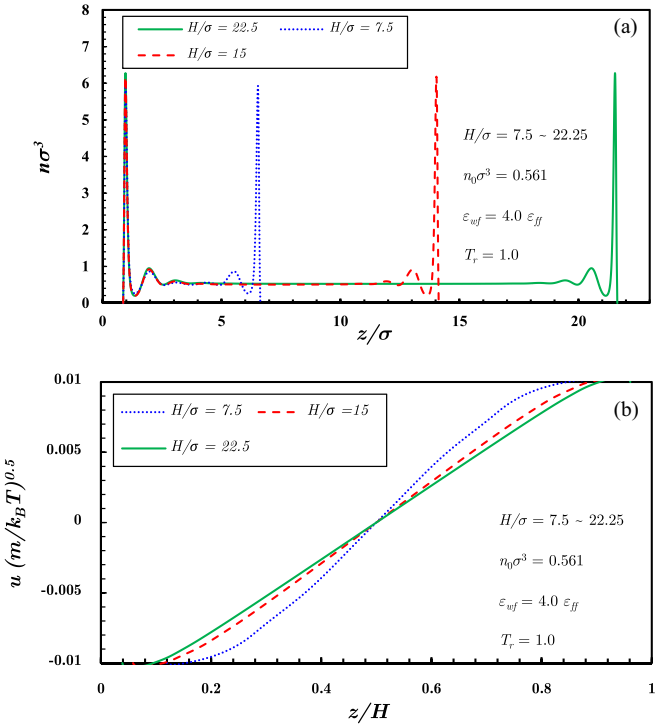

FIG. 5. Effects of channel width on density (a) and velocity (b) profiles of Couette flow with the 10-4-3 wall potential.

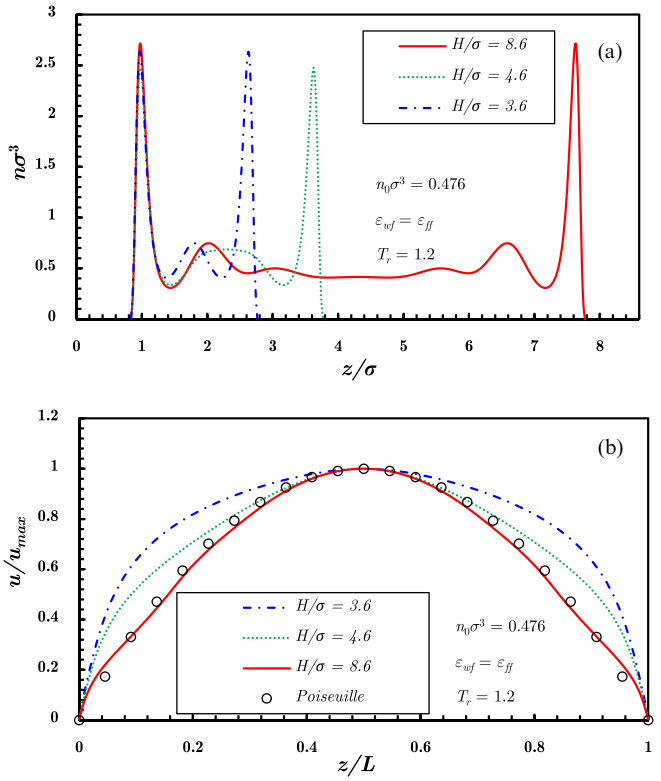

FIG. 6. Density (a) and velocity (b) profiles under different channel-width conditions for Poiseuille flow, where $L = H - 2\delta$.

velocities distributed in $[-4\sqrt{2k_BT/m}, 4\sqrt{2k_BT/m}]$ are used to discretize the velocity space in each direction. Although the local Knudsen number can be very high, as will be discussed later, the set of 8×8 discretized velocities is sufficient to capture the nonequilibrium effects of the current problem, as we have tested. The Courant-Friedrichs-Lewy (CFL) number is set to be 0.1. The fluid is confined between two 10-4 walls with a separation of $H = 7.178\sigma$, in which the pore-averaged density of the confined fluids is $n_0 = 0.593\sigma^{-3}$ with the temperature of $T_r = 1.0$.

The static structure and dynamic behaviors of the LJ fluids for Couette flow are also satisfactorily captured by the current DUGKS compared to the MD results [55], as shown in Fig. 4. Three adsorption layers with decreasing intensity are observed in the vicinity of each wall, while there is no obvious bulk region near the center of the channel [Fig. 4(a)]. As shown in Fig. 4(b), the velocity distribution of Couette flow deviates from linearity, as a result of fluid inhomogeneity induced by the competition of the wall-fluid and fluid-fluid interactions. Thus, it is essential to take the wall potentials and fluid molecule interactions into account at the nanometer scale, which greatly affects the density [Fig. 4(a)] and velocity [Fig. 4(b)] distributions across the channel.

The effects of flow channel widths on density and velocity distribution of Couette flow are also investigated. In the simulation, the top and bottom plates move with a velocity of $U = 0.01\sqrt{k_BT/m}$ in opposite directions. The confined fluids, with an averaged density of $n_0 = 0.561\sigma^{-3}$ at the temperature of $T_r = 1.2$, are simulated with the 10-4-3 potentials from the top and bottom walls, respectively. Meanwhile, the energy parameter of the wall-fluid interactions ε_{wf} is four times that for fluid-fluid interactions ε_{ff}. As is shown in Fig. 5, there are two obvious adsorption layers in the vicinity of each wall, after which a weakly third adsorption layer occurs. All three adsorption layers coincide together, indicating a similar effect is exerted on fluid molecules from the wall. The bulk region increases with the channel width H increasing. The velocity profile tends to be linearly distributed across the channel with the increase of the channel widths H [Fig. 5(b)]. This is because the inhomogeneity of the fluid system becomes weaker in larger scale systems. It also means that there is a critical value for the channel width, over which the inhomogeneity of the system can be ignored. The determination of the critical value will be studied in the future.

2. *Poiseuille flow*

Finally, we take the Poiseuille flow as our third test case. Adopting the same parameters as presented in Fig. 3(b) and exerting a driving force of $G_x = 0.02\varepsilon_{ff}/\sigma$ in the x direction, the previous static problem transforms into the Poiseuille flow.

The Poiseuille flow is studied under different channel-width conditions. As shown in Fig. 6(a), the density fluctuates across the whole flow domain as $H = 3.6\sigma$, while a bulk region may occur with the increase of channel width. This is because the competition between the solid-fluid and fluid-fluid interactions becomes weaker near the center region of a larger channel, and the influences from the wall are limited. In Fig. 6(b), the velocity is normalized by the maximum velocity $u_{\max}$ and the distance is normalized by effective flow domain length $L = H - 2\delta$. As we can see, the velocity profile approaches the Navier-Stokes solution with the increase of the channel width, which further supports our assessment that the fluid system becomes more homogeneous in large systems.

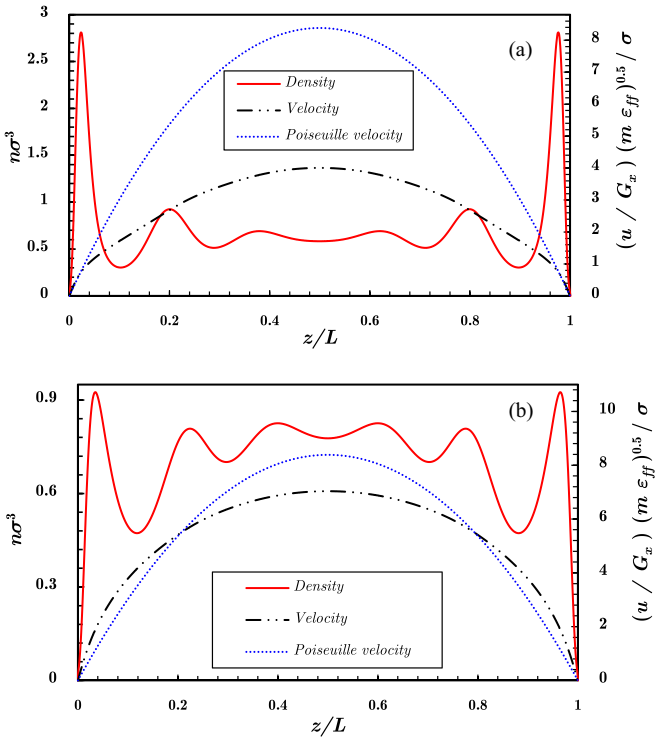

FIG. 7. The density and velocity profiles for Poiseuille flow in confined 10-4-3 LJ channels at the temperature of $T_r = 1.2$: (a) wetting case, $\varepsilon_{wf}/\varepsilon_{ff} = 1.0$; (b) nonwetting case, $\varepsilon_{wf}/\varepsilon_{ff} = 0.25$. The velocity profiles were normalized by the external driving force G_x. The pore-averaged density is $0.561\sigma^{-3}$ and the channel with is 7.5σ. The locations were normalized by the length of the flow domain $L = H - 2\delta$.

The density and velocity profiles for Poiseuille flow with the wall separation of $H = 7.5\sigma$ at the temperature of $T_r = 1.2$ are shown in Fig. 7, where the velocity is normalized by the external driving force G_x and the location is normalized by the flow domain L. For the wetting case ($\varepsilon_{wf}/\varepsilon_{ff} = 1.0$), fluid molecules accumulate near the wall due to the strong solid-fluid interactions, and the velocity is much smaller than the analytical Poiseuille solution across the channel. When the ratio $\varepsilon_{wf}/\varepsilon_{ff}$ decreases to 0.25, the walls become nonwetting, and the density oscillation becomes much flatter, compared to the wetting case in Fig. 7(a). However, the adsorption layers near the wall still exist, but with much smaller magnitude. Meanwhile, the velocity becomes much higher than that under wetting conditions, implying a significant effect of wettability on flow velocity.

We want to point out that the computational efficiency of the DUGKS is much higher than that of the MD simulations. In one of our test cases of the Poiseuille flow under the same working condition, the computing time of the DUGKS running with a single core is about 10 min, while it is more than 7 h of MD simulations running with 24 cores to obtain satisfactorily stable results.

3. Multiscale characteristics of a dense fluid system

The Knudsen number is commonly used as a key criterion number in multiscale analysis from continuum flow to free molecular flow in rarefied gas dynamics. However, fluid molecular movements are frequently disrupted by the walls or other molecules due to the small dimension of the flow path or the dense arrangements of the fluid molecules in the case we study, which means that the molecules cannot move freely. Thus, the Knudsen number in this paper is actually the effective Knudsen number, which is borrowed from rarefied gas dynamics for the current dense fluid system. According to the difference in defining the characteristic lengths, the average effective Knudsen number Kn and local effective Knudsen number Kn* can be defined as

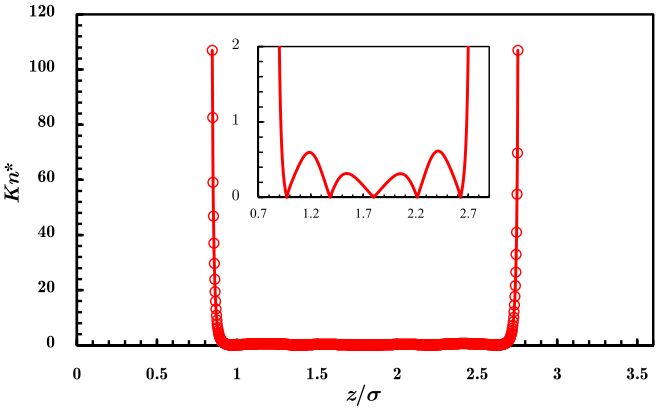

FIG. 8. The variation of local effective Knudsen number across the channel with the 10-4-3 potential, where $H/\sigma = 3.6$, $n\sigma^3 = 0.476$, $T_r = 1.2$, and $\varepsilon_{wf} = \varepsilon_{ff}$.

$$\mathrm{Kn} = \frac{\lambda}{H}, \quad \mathrm{Kn}^* = \frac{\lambda}{\rho/|\nabla\rho|}, \tag{44}$$

where λ is the gas mean free path, and $\rho/|\nabla\rho|$ is the local characteristic length. According to dense gas theory [4,23], the mean free path is determined by

$$\lambda = \frac{1}{\sqrt{2}n\pi\sigma^2\chi}. \tag{45}$$

On one hand, the average effective Knudsen number is calculated as Kn = 0.06, according to Eq. (44) and the parameters in Fig. 3(b), from which we may deduce that the nonequilibrium effects are not very obvious; on the other hand, the density varies sharply near the wall, resulting in an enormous local characteristic length, where the local effective Knudsen number can be as high as 106.976. Beyond that, it is almost smaller than 0.5 near the center region, and even as small as 0.000 58 in certain places. The violent fluctuation of the local effective Knudsen number, as shown in Fig. 8, implies the strong inhomogeneity of the dense fluid system across the channel.

Meanwhile, the mechanism of rarefaction effect in a dense fluid system may be very different from that in a rarefied one. For the Poiseuille flow of rarefied gases, the rarefaction effect mainly occurs at the gas-solid interface showing as a velocity slip, which is attributed to the infrequent collisions between the gas and solid molecules. However, the density is strongly inhomogeneous in dense fluid systems, which means the amount of gas molecules between the adjacent adsorption layers is very small, even close to the vacuum,

where the rarefaction effect may occur, rather than at the fluid-solid interface. The detailed mechanism of rarefaction effect in a dense fluid system is very complicated, and needs deeper investigation in the future. According to our test cases, the velocity profile does not converge using lower-order Gauss-Hermite quadrature of velocity space, for example, four discretized velocity points in the x and y directions, respectively. This phenomenon suggests rarefaction effects do exist in a dense fluid system and the system is a multiscale one. The numerical results demonstrate the capability of the DUGKS in simulating fluid flows for all the effective Knudsen numbers.

V. CONCLUSIONS

It is a challenging task to capture the nonequilibrium effects of dense fluid flows at the nanometer scale. In this paper, the DUGKS is extended to strongly inhomogeneous fluid systems, where the external wall potential, volume exclusion effects, and long-range intermolecular attractions are simultaneously taken into account. These nonequilibrium effects are coupled into a unified force term, which is conveniently incorporated into the DUGKS by the Strang splitting method. The time step of the DUGKS is not limited by particle collision time in multiscale flow regimes, which indicates that the DUGKS is an ideal tool to simulate dense fluid flow dynamics, since the effective Knudsen number may vary significantly under different conditions.

The static fluid structures and dynamic flow behaviors agree well with Monte Carlo simulation and/or MD results, which proves the capability of our model to capture the nonequilibrium effects of dense fluid systems at the nanometer scale where the local effective Knudsen number can vary from the order of 0.0001 to the order of 100. There will be a vacuum between the first fluid layer and the wall due to the strong repulsion, while several adsorption layers may occur due to the competition of solid-fluid and fluid-fluid interactions. It is also found that the density distribution across the channel is not affected by the fluid flow. The velocity profile of the Couette flow deviates from the linear distribution, while the velocity profile of Poiseuille flow deviates from the Navier-Stokes solution significantly as a result of the inhomogeneous nature of the dense fluids at the nanometer scale.

In our future work, more practical boundary conditions will be considered to propose in the future, which may serve as a powerful tool between the connections of MD simulation and the Navier-Stokes equation.

ACKNOWLEDGMENTS

This work was supported by the National Science Foundation of China (Grant No. 51836003). Y.Z. would like to thank the UK's Engineering and Physical Sciences Research Council for financial support under Grant No. EP/M021475/1. Helpful discussions with Dr. Songze Chen and valuable advice from him are highly appreciated.

[1] L. Wu, Y. Zhang, and J. M. Reese, J. Comput. Phys. **303**, 66 (2015).
[2] A. V. Raghunathan, J. H. Park, and N. R. Aluru, J. Chem. Phys. **127**, 174701 (2007).
[3] J. Badur, P. Ziółkowski, S. Kornet, T. Kowalczyk, K. Banaś, M. Bryk, P. J. Ziółkowski, and M. Stajnke, J. Theor. Appl. Mech., **56**, 329 (2018).
[4] L. Wu, H. Liu, J. M. Reese, and Y. Zhang, J. Fluid Mech. **794**, 252 (2016).
[5] L. Zhang, B. Shan, Y. Zhao, and Z. Guo, Int. J. Heat. Mass. Transfer **139**, 144 (2019).
[6] C. Wang, Y. V. Kaneti, Y. Bando, J. Lin, C. Liu, J. Li, and Y. Yamauchi, Mater. Horiz. **5**, 394 (2018).
[7] M. A. Shannon, P. W. Bohn, M. Elimelech, J. G. Georgiadis, B. J. Marinas, and A. M. Mayes, Nature **452**, 301 (2008).
[8] K. Buruga, J. T. Kalathi, K. Kim, Y. S. Ok, and B. Danil, J. Ind. Eng. Chem. **61**, 169 (2018).
[9] Z. Guo, T. S. Zhao, C. Xu, and Y. Shi, Int. J. Comput. Fluid Dyn. **20**, 361 (2006).
[10] L. Chen, J. Wen, P. Zhang, B. Yu, C. Chen, T. Ma, X. Lu, S. H. Kim, and L. Qian, Nat. Commun. **9**, 1542 (2018).
[11] J. D. Figueroa, T. Fout, S. Plasynski, H. McIlvried, and R. D. Srivastava, Int. J. Greenhouse Gas Control **2**, 9 (2008).
[12] M. Konarova, A. Tanksale, J. N. Beltramini, and G. Q. Lu, Nano Energy **2**, 98 (2013).
[13] B. Li, H. M. Wen, Y. Yu, Y. Cui, W. Zhou, B. Chen, and G. Qian, Mater. Today Nano **2**, 21 (2018).
[14] Y. Zhang, L. Zhu, R. Wang, and Z. Guo, Phys. Rev. E **97**, 053306 (2018).
[15] K. Xu and J. Huang, J. Comput. Phys. **229**, 7747 (2010).
[16] Z. Guo, J. Qin, and C. Zheng, Phys. Rev. E **89**, 013021 (2014).
[17] S. Shen, G. Chen, R. M. Crone, and M. Anaya-Dufresne, Phys. Fluids **19**, 086101 (2007).
[18] W. Zhang, G. Meng, and X. Wei, Microfluid. Nanofluid. **13**, 845 (2012).
[19] K. P. Travis and K. E. Gubbins, J. Chem. Phys. **112**, 1984 (2000).
[20] S. Roy, R. Raju, H. F. Chuang, B. A. Cruden, and M. Meyyappan, J. Appl. Phys. **93**, 4870 (2003).
[21] M. Kazemi and A. Takbiri-Borujeni, Int. J. Coal Geol. **146**, 188 (2015).
[22] Z. Guo, T. S. Zhao, and Y. Shi, Phys. Rev. E **71**, 035301(R) (2005).
[23] S. Chapman and T. G. Cowling, *The Mathematical Theory of Non-uniform Gases* (Cambridge University Press, Cambridge, 1970).
[24] H. Van Beijeren and M. H. Ernst, Physica (Amsterdam) **68**, 437 (1973).
[25] J. Karkheck and G. Stell, J. Chem. Phys. **75**, 1475 (1981).
[26] M. Grmela, J. Stat. Phys. **3**, 347 (1971).
[27] M. Sadr and M. H. Gorji, J. Comput. Phys. **378**, 129 (2019).
[28] H. T. Davis, J. Chem. Phys. **86**, 1474 (1987).
[29] T. K. Vanderlick, L. E. Scriven, and H. T. Davis, J. Chem. Phys. **90**, 2422 (1989).

[30] T. K. Vanderlick and H. T. Davis, J. Chem. Phys. **87**, 1791 (1987).
[31] Z. Guo, K. Xu, and R. Wang, Phys. Rev. E **88**, 033305 (2013).
[32] G. R. McNamara and G. Zanetti, Phys. Rev. Lett. **61**, 2332 (1988).
[33] Z. Guo, R. Wang, and K. Xu, Phys. Rev. E **91**, 033313 (2015).
[34] P. Wang, S. Tao, and Z. Guo, Comput. Fluids **120**, 70 (2015).
[35] Z. Guo and K. Xu, Int. J. Heat Mass Transfer **102**, 944 (2016).
[36] X. Luo and H. Yi, Int. J. Heat Mass Transfer **114**, 970 (2017).
[37] C. Zhang and Z. Guo, Int. J. Heat Mass Transfer **134**, 1127 (2019).
[38] L. Zhu and Z. Guo, Comput. Fluids **193**, 103613 (2019).
[39] H. Liu, Y. Cao, Q. Chen, M. Kong, and L. Zheng, Comput. Fluids **167**, 313 (2018).
[40] Y. Huo and Z. Rao, Int. Commun. Heat Mass **91**, 187 (2018).
[41] C. Zhang, K. Yang, and Z. Guo, Int. J. Heat Mass Transfer **126**, 1326 (2018).
[42] Z. Guo, J. Li, and K. Xu, arXiv:1909.04923.
[43] J. W. Dufty, A. Santos, and J. J. Brey, Phys. Rev. Lett. **77**, 1270 (1996).
[44] Z. Guo, T. S. Zhao, and Y. Shi, Phys. Fluids **18**, 067107 (2006).
[45] P. Tarazona, Phys. Rev. A **31**, 2672 (1985).
[46] N. F. Carnahan and K. E. Starling, J. Chem. Phys. **51**, 635 (1969).
[47] W. A. Steele, Surf. Sci. **36**, 317 (1973).
[48] X. He, X. Shan, and G. D. Doolen, Phys. Rev. E **57**, R13(R) (1998).
[49] J. A. Barker and D. Henderson, J. Chem. Phys. **47**, 4714 (1967).
[50] R. L. Cotterman, B. J. Schwarz, and J. M. Prausnitz, AIChE J. **32**, 1787 (1986).
[51] G. Strang, SIAM J. Numer. Anal. **5**, 506 (1968).
[52] S. Tao, H. Zhang, Z. Guo, and L. Wang, J. Comput. Phys. **375**, 498 (2018).
[53] P. Wang, M. T. Ho, L. Wu, Z. Guo, and Y. Zhang, Comput. Fluids **161**, 33 (2018).
[54] B. Van Leer, J. Comput. Phys. **23**, 276 (1977).
[55] I. Bitsanis, J. J. Magda, M. Tirrell, and H. T. Davis, J. Chem. Phys. **87**, 1733 (1987).
[56] K. Wu, Z. Chen, J. Li, X. Li, J. Xu, and X. Dong, Proc. Natl. Acad. Sci. USA **114**, 3358 (2017).
[57] I. Bitsanis, S. A. Somers, H. T. Davis, and M. Tirrell, J. Chem. Phys. **93**, 3427 (1990).
[58] I. K. Snook and W. van Megen, J. Chem. Phys. **72**, 2907 (1980).